Asymmetric Positioning for NLOS Mitigation

Qiming Zhong
University College London, United Kingdom

BIOGRAPHY

Qiming Zhong is a PhD student at University College London (UCL), specializing in 3D-mapping-aided GNSS. He holds a BSc in Electrical and Electronic Engineering from the University of Nottingham, Ningbo, China and an MSc in Robotics and Computing from UCL. (q.zhong.17@ucl.ac.uk)

ABSTRACT

Conventional GNSS positioning algorithms rely on the assumption that the pseudo-range error follows a normal distribution, which allows for the use of statistical techniques and probabilistic models to improve the accuracy and reliability of the positioning solution. However, this assumption does not always hold true in practice, especially in urban environments where blocking, reflections, and other factors can significantly impact the quality of the GNSS signals and lead to errors that do not conform to a normal distribution. In this paper, an efficient NLOS mitigation algorithm is proposed to improve positioning performance in cities. It allows conventional least-squares ranging (LSR) and extended Kalman filtering (EKF) to handle asymmetric distributions and to determine an appropriate distribution for each measurement based on its signal strength. This algorithm can be implemented on any GNSS receiver with only a small increase in processing load, and it does not require any additional information or hardware. The experiments were conducted in 13 different locations alongside busy roads in the London Borough of Camden, where two 3-minute sessions of static pedestrian navigation data were collected at each location using a u-blox ZED-F9P GNSS receiver, one for training and the other for testing. The experimental results confirm that the pseudo-range error of the NLOS signal does not conform to a normal distribution. Compared to the conventional approaches, the proposed method was able to reduce the RMS horizontal position error by about 21% and 34% in the single and multi-epoch cases, respectively. The performance of the proposed method was also compared to 3D-mapping-aided (3DMA) GNSS positioning.

I. INTRODUCTION

Navigation and positioning are crucial in modern society, and Global Navigation Satellite System (GNSS) technology is widely used for these purposes in the outdoors. The demand for and potential of navigation and positioning services in urban areas is significant. Location-based services and applications have become integrated into various aspects of people's lives, such as travel, entertainment, and health (Usman et al., 2018). In recent years, positioning modules have been included in a variety of consumer products, such as smartwatches and smartphones, allowing for easy access to location information. The incorporation of location information has improved the user experience of existing applications, while also giving rise to new ones. These services and applications also increase the demand for positioning methods for consumer-level equipment that can achieve meters-level horizontal accuracy without requiring additional computing resources or power consumption (European GNSS Agency, 2018). However, the performance of GNSS in urban environments is not satisfactory, as indicated by a survey of Android customers in 2018 which found that poor positioning performance in cities is a primary concern for users (van Diggelen, 2021).

There are many reasons for the poor performance of GNSS in urban areas. One obvious issue is the presence of tall buildings that can block part of the satellite signals, leaving only a small part of the sky overhead unblocked, leading to a reduced number of available satellites and poor geometric distribution. However, in recent years, the progressive completion of the deployment of Galileo and Beidou constellations has increased the number of available satellites, alleviating this problem to some extent. In addition, reflection effects can interfere with GNSS positioning. In cities, especially emerging ones, the rise of modern architectural styles using tempered glass for facades makes these buildings powerful radio reflectors that can easily reflect GNSS signals.

The most commonly mentioned causes of limited performance of conventional GNSS positioning in cities are multipath interference and non-line-of-sight (NLOS) reception, which occur frequently in such environments. Multipath interference occurs when the user receives a mixture of direct line-of-sight (LOS) satellite signals and corresponding reflected replicas from smooth buildings and the ground simultaneously (Misra and Enge, 2010; Groves, 2013; Ward et al., 2017; McGraw et al., 2020). This causes the resultant signal received by the receiver to be distorted, leading to errors in pseudo-range, carrier phase, Doppler shift and signal strength measurements. NLOS reception occurs when the LOS signal is blocked and the user can only receive reflected replicas. As reflections may significantly increase the signal propagation path, NLOS reception will introduce

considerable positive errors, reaching tens of metres and even hundreds of metres in some extreme cases. The strength of NLOS signals can vary greatly, with some being weak and others almost as strong as normal LOS signals (Groves et al., 2013; Groves and Jiang, 2013; Wang, 2015).

There are several methods available for mitigating the effects of multipath interference and NLOS reception in GNSS positioning. These methods can be broadly classified as antenna-based techniques, receiver-based techniques, and post-receiver techniques (also known as navigation processor-based techniques) (Groves, 2013; Zidan et al., 2021). In some studies, these techniques mentioned above are used in combination (Groves, 2013).

Antenna-based techniques usually have large antenna structures with good polarisation differentiation, which can significantly reduce positioning errors caused by multipath interference by attenuating reflected signals (Groves and Jiang, 2013). However, it has no significant effect on the pseudo-range errors caused by NLOS reception (Groves and Jiang, 2013). In addition, they are not suitable for most applications where small and low-cost antennas are required (Zidan et al., 2021).

Receiver-based techniques increase the discrimination of the code correlation function by modifying the design of the discriminator, resulting in reduced code tracking errors and path delays due to multipath interference (Hsu et al., 2015b). But for NLOS mitigation, they are less effective (Hsu et al., 2015b; Groves and Jiang, 2013). Moreover, they increase the cost and energy consumption of the receiver (Groves and Jiang, 2013).

Post-receiver techniques act on pseudo-range, carrier phase, signal strength and Doppler measurements. Incorporating additional information, based on 3D mapping data (Groves et al., 2020; Zhong and Groves, 2022b) and inertial navigation systems (INS) (Wang et al., 2022; Zhang et al., 2020), could reduce the impact of NLOS reception and multipath on the GNSS positioning results to some extent (Zidan et al., 2021). However, they increase operational costs and require more computing resources to process the additional data. Without additional information, a consistency check of the pseudo-range is commonly used to detect the measurements contaminated by NLOS reception and multipath interference (Zidan et al., 2021), most of which simply discard the contaminated measurements.

Conventional GNSS positioning algorithms, such as least-squares estimation and extended Kalman filtering (EKF), are widely used to determine the position of a receiver based on signals received from a network of GNSS satellites (Groves, 2013). These algorithms rely on the assumption that the pseudo-range error, which represents the difference between the observed and true range between the receiver and a satellite after correction for known errors such as satellite clock offsets and atmospheric delays, follows a normal distribution. This assumption allows for the use of statistical techniques and probabilistic models to improve the accuracy and reliability of the positioning solution.

However, this assumption may not always hold true in practice, especially in urban environments where, as mentioned above, blocking, reflections, and other factors can significantly impact the quality of the GNSS signals and lead to pseudo-range errors that do not conform to normal distribution. As a result, these conventional algorithms may not perform optimally in cities, resulting in degraded positioning accuracy and reliability. This paper introduces a post-receiver approach that corrects NLOS errors by providing a better model of the statistical distribution for NLOS signals with a small increase in computational load and without the need for additional information or hardware.

There are many applications that could benefit from this work. Those applications that use GNSS ranging to compute user location, such as navigation for pedestrians and vehicles, emergency call location for people and vehicles, navigation for the visually impaired, location-based services, mobile gaming, etc, are able to gain performance improvements without the need for additional information or hardware. Other ranging-based positioning applications, such as Wi-Fi indoor positioning using Round Trip Time (RTT) (Gentner et al., 2020), could also gain some ideas and inspiration from this work.

This paper has been divided into 5 sections. Section II reviews various NLOS mitigation methods. Then, in Section III, the likelihood-based NLOS mitigation method designed according to the characteristics of the NLOS pseudo-range error distribution is described in detail, followed by a description of how this algorithm can be mounted to positioning algorithms. Section IV presents the test results of a GNSS dataset collected from multiple test sites in London. A comparison of positioning results using different NLOS mitigation methods is shown, with solutions from conventional GNSS positioning used as a reference. Finally, the conclusions are summarised in Section V.

II. BACKGROUND

II.1. Conventional GNSS Positioning

Location-based services usually use single-epoch positioning, for which non-linear least-squares estimation is commonly employed to calculate a position solution from a set of simultaneous GNSS measurements. The least-squares ranging begins with state prediction, followed by the modelling of pseudo-range measurements and calculation of measurement innovations. The measurement matrix linking the state and measurement domains is then calculated, and the state estimate is updated through least-squares. This process is repeated until the change in the state estimate between iterations falls below a predetermined

threshold. In practice, some measurements are more accurate than others. For example, measurements of strong signals tend to have smaller errors than weak ones. Therefore, in the least-squares ranging, measurement innovations are usually weighted based on the signal strength and/or satellite elevation, with more accurate measurements given greater weight to obtain the best state estimate (Groves, 2013).

All road and pedestrian navigation applications use filtered solutions. Filtering algorithms use new measurements to correct navigation solutions predicted from previous information. Kalman filter-based estimation techniques are commonly used in navigation. It uses information about the deterministic and statistical characteristics of system parameters and measurements to determine the optimal state estimates based on available data. It is a Bayesian estimation technique with two phases, starting with an initial set of state estimates and operating recursively to update these estimates and their associated error covariances using the latest measurement and an appropriate mathematical model. The extended Kalman filter, which is a standard approach for multi-epoch GNSS positioning, is a non-linear version of the Kalman filter that uses Taylor's theorem to linearise the state transition and observation model (Groves, 2013).

II.2. NLOS Detection and Mitigation

In urban canyons, multipath interference and NLOS reception occur frequently (Groves, 2013), and have been considered to be the two key reasons that restrict the performance of conventional GNSS positioning (Kaplan and Hegarty, 2017; Ng et al., 2021; Hsu et al., 2015b; Groves, 2013; Yuan et al., 2020; Groves et al., 2013).

Various methods of distinguishing the NLOS from the LOS signals have been proposed. Some researchers have explored the use of more advanced hardware, such as the dual-polarization antenna to separately process the right-handed circularly polarization (RHCP) and left-handed circularly polarization (LHCP) components of the signal (Jiang and Groves, 2014; Egea-Roca et al., 2018) and the antenna array to measure the angle of arrival (Keshvadi et al., 2011; Vagle et al., 2017), to better detect NLOS. Additional equipment can be used to assist with NLOS detection. For example, cameras can be used to obtain a plot of the sky at the current location to determine which signals are obscured and which are not (Meguro et al., 2009; Marais et al., 2014). The study in (Wen et al., 2021) uses a light detection and ranging (LiDAR) sensor to identify obstacles that may block the direct transmission path of satellite signals.

In addition to hardware, some additional information can be used to detect NLOS measurements, of which 3D mapping data is a frequently mentioned one. The emergence of 3D mapping data provides additional information for navigation and positioning, and also enriches methods for dealing with issues such as multipath and NLOS reception. Those 3D models are often used to predict, at any given location, which satellite signals are directly visible and which are blocked by obstacles, and even in some implementations, to estimate path delays. The methods for implementing 3DMA GNSS are flexible and varied. In the past few years, many different 3D-mapping-aided (3DMA) GNSS techniques, e.g., (Groves et al., 2020; Hsu et al., 2016; Ziedan, 2017; Ng et al., 2020; Suzuki and Kubo, 2013; Wang et al., 2015; Suzuki, 2016; Ziedan, 2019; Zhong and Groves, 2022b,a), have been demonstrated to significantly improve the performance of GNSS in cities.

In the absence of both additional information and hardware, some studies (Groves and Jiang, 2013; Hsu et al., 2017; Hsu, 2017; Yozevitch et al., 2016) have focused on using the measurement data itself to distinguish between LOS and NLOS. Signal strength and elevation angle are usually used as important bases for determining LOS and NLOS signals. NLOS signals are on average less intense than LOS ones, and satellites with high elevations are less likely to be obscured. However, there are inevitable exceptions, where NLOS signals reflected by smooth surfaces may be almost as strong as LOS signals, and satellites along the street direction may be not obscured even if their elevation is not high.

Another option is consistency checking, which works on the assumption that NLOS measurements produce less consistency than LOS measurements. A common approach is "top-down" sequential testing, where one measurement with the largest residual is excluded at each iteration until the residuals of the rest measurements are less than a threshold. An alternative to the "top-down" sequential testing approach is the "bottom-up" subset comparison (Groves and Jiang, 2013). The "bottom-up" method starts by taking a subset of measurements and then expands the subset by adding additional measurements that are consistent with it. The quality of the subset is important for this type of method, as a minimal subset contaminated with faulty observations may directly degrade the performance of outlier detection.

In addition, with the popularity of artificial intelligence and machine learning in recent years, many researchers have tried to use them to classify LOS and NLOS signals. Examples include decision trees (Yozevitch et al., 2016; Sun et al., 2019), support vector machines (SVM) (Hsu, 2017; Lyu and Gao, 2020), and fully convolutional networks (FCN) (Lyu and Gao, 2020), while features commonly used for training include signal strength, satellite elevation, pseudo-range, pseudo-range drift, derivative of pseudo-range, etc.

There are several ways to mitigate the impact of NLOS signals on GNSS positioning performance, including weighting, exclusions, and corrections, each of which has advantages and disadvantages. Applying different weights to measurements in the calculation to optimise the position estimate is commonly used as a standard method in many studies (Groves, 2013).

This reduces, but does not eliminate, the influence of NLOS signals on the positioning results. The weights usually depend on the strength of the signal, the elevation angle of the satellite, and even, in some studies (Zhong and Groves, 2022b), the LOS probability of the signal. In order to completely eliminate the contamination of the position solution by significant NLOS measurements, those measurements can be directly excluded from the calculation. Examples include (Jiang and Groves, 2014; Hsu et al., 2015a; Wen et al., 2021) However, the risk of this scheme is that some good measurements may be excluded because the results of the NLOS detection are not always correct. It also cuts down the number of signals involved in the calculation and may result in a deterioration of the satellite geometry, which eventually leads to a degradation of performance. The final option is to correct the NLOS measurements using some additional information, such as 3D mapping and LiDAR, and retain them in the calculation of the position solution, which maximises the use of all received measurements and also avoids potential degradation of the satellite geometry. Examples include (Ziedan, 2017; Ng et al., 2020; Miura et al., 2015; Wen and Hsu, 2022) However, when the corrections are wrong, instead of giving a performance improvement, this may reduce the accuracy of the positioning results.

III. PROPOSED METHODS

III.1. NLOS Mitigation Algorithm

The NLOS Mitigation Algorithm (NLOSMA) applies different statistical distributions to pseudo-range errors based on satellite signal strength, which are then remapped to a normal distribution to calculate pseudo-range corrections. The remapping step follows the same procedure as the likelihood-based ranging described in (Zhong and Groves, 2022b), but neither 3D mapping aiding nor scoring of a grid of candidates is used here. In addition, it contains an outlier detection module to label those measurements for which the pseudo-range innovation remains significantly large after remapping. Figure 1 shows the components of the proposed algorithm. It can be implemented without significant changes to the main structure of the existing least-squares ranging or extended Kalman filtering process. This can help to minimize the impact on system complexity, computational cost and power consumption, making it suitable for real-time applications. The proposed method also does not require a communications link to a server.

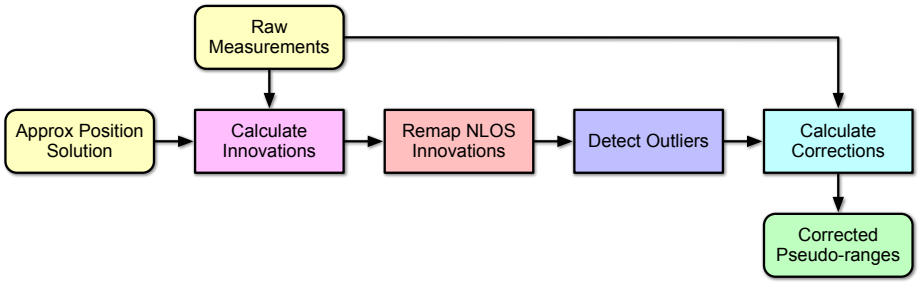

Figure 1: Components of the NLOS mitigation algorithm (NLOSMA)

The proposed algorithm, NLOSMA, in Figure 1 requires an approximate position of the user receiver, which could be obtained in various ways, such as least-squares ranging and position prediction in filters. Once this initial receiver position estimate has been obtained, the NLOS mitigation algorithm comprises the following steps:

1. At a given user receiver position, it is difficult to discern which satellites are LOS and which are NLOS unless additional information (e.g., 3D mapping data and camera images) is available. Therefore, the visibility of a satellite can only be inferred from its measured C/N_0 value. Measurement j is assumed to be a LOS signal when the following condition is met
$$(C/N_0)_j > T_{C/N_0} \tag{1}$$
where T_{C/N_0} is the cutoff value for the LOS and NLOS signals. The reference satellite is the one with the highest C/N_0 value.

2. At the given receiver position, the measured pseudo-ranges are corrected for any known errors other than NLOS path delay, such as atmospheric delays, satellite clock offsets, and inter-constellation clock offsets. The measurement innovation is then derived by subtracting the predicted range between the corresponding satellite and the predicted receiver position, from the corrected pseudo-ranges. The measurement innovation is finally differenced with respect to the reference satellite to eliminate the receiver clock offset.
$$\Delta\delta z_{pj} = (\rho_{j,C} - r_{aj}) - (\rho_{r,C} - r_{ar}) \tag{2}$$

where $\rho_{j,C}$, r_{aj}, $\rho_{r,C}$, and r_{ar} are, respectively, the corrected pseudo-range for satellite j, the predicted range for satellite j, the corrected pseudo-range for the reference, and the predicted range for the reference. The error standard deviation of all errors except for the NLOS path delay is computed as a function of C/N_0 using,

$$\sigma_j^2 = a \times 10^{-(C/N_0)_j/10} + b + \sigma_r^2 \tag{3}$$

where a and b are empirically determined constants, and σ_r is the error standard deviation of the reference satellite.

3. At the given receiver position, the measurement innovations for satellites predicted to be LOS are modelled by a symmetric distribution, while those for satellites predicted to be NLOS are modelled by an asymmetric distribution. In this paper, a normal distribution with a mean of μ_L is used for LOS signals, and a skew-normal distribution with the location, ξ_N, scale, ω_N and shape, α_N, is used for NLOS signals, as follows (Zhong and Groves, 2022b),

$$\xi_N = \mu_L + \mu_N - \sqrt{\frac{2\sigma_N^2\left(\sigma_j^2 + \sigma_N^2\right)}{\pi\sigma_j^2 + (\pi - 2)\sigma_N^2}} \tag{4}$$

$$\omega_N = \sqrt{\frac{\left(\sigma_j^2 + \sigma_N^2\right)^2}{\sigma_j^2 + (1 - 2/\pi)\,\sigma_N^2}} \tag{5}$$

$$\alpha_N = \sqrt{\frac{\sigma_N^2}{\sigma_j^2}} \tag{6}$$

whereμ_N and σ_N are the mean and standard deviation of the NLOS path delay, respectively. The cumulative probability, F, of the NLOS measurement innovation, $\Delta\delta z_{pj}$, is then computed using

$$F = \frac{1}{2}\left[1 + \mathrm{erf}\left(\frac{\Delta\delta z_{pj} - \xi_N}{\omega_N\sqrt{2}}\right)\right] - 2T\left(\frac{\Delta\delta z_{pj} - \xi_N}{\omega_N}, \alpha_N\right) \tag{7}$$

where $\mathrm{erf}(x)$ is the integral of the normal distribution and $T(x, \alpha)$ is Owen's T function. The modified measurement innovation, $\Delta\delta z'_{pj}$, is then obtained by solving

$$F = \frac{1}{2}\left[1 + \mathrm{erf}\left(\frac{\Delta\delta z'_{pj}}{\sqrt{2\sigma_j^2}}\right)\right] \tag{8}$$

For measurements predicted to be LOS, the measurement innovation remains unchanged, i.e., $\Delta\delta z'_{pj} = \Delta\delta z_{pj}$.

4. The modified innovations are normalised and each is then compared to a threshold value. Measurement j is an outlier when the following condition is met

$$\left|\frac{\Delta\delta z'_{pj} - \mu_L}{\sigma_j}\right| > T_{\delta z} \tag{9}$$

where $T_{\delta z}$ is the outlier detection threshold. When the number of remaining measurements is less than the minimum number, k, for determining the positioning solution, the k measurements with the smallest residuals will be retained.

5. The corrected pseudo-range measurement, $\rho'_{j,C}$, can be obtained by

$$\rho'_{j,C} = \rho_{j,C} + \left(\Delta\delta z'_{pj} - \Delta\delta z_{pj}\right) \tag{10}$$

The determination of the parameters is described in Section IV.2, and their values are summarised in Table 2.

III.2. Single-Epoch Least-Squares Ranging

The conventional least-squares ranging (LSR) with terrain height aiding used in this paper is described in detail in Appendix A.1. As shown in Figure 2, NLOSMA can be easily incorporated into the conventional LSR, as once an approximate position solution is obtained, the pseudo-ranges can be corrected using the method in Section III.1 to take effect in the next iteration

of least-squares. Since the pseudo-range correction calculated by NLOSMA is related to the approximate position solution, it needs to be iterated with the least-squares estimate until the solution converges or the maximum number of iterations is reached.

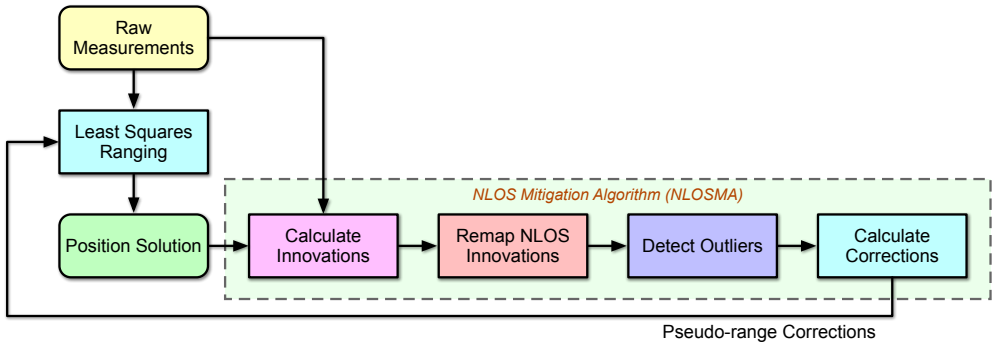

Figure 2: Components of the least-squares ranging with NLOS mitigation algorithm

III.3. Multi-Epoch Extended Kalman Filtering

A detailed description of the conventional extended Kalman filtering (EKF) algorithm with terrain height aiding can be found in Appendix A.2. Figure 3 shows the way in which NLOSMA is incorporated within the conventional EKF. The conventional EKF works by a two-phase process, namely system propagation and measurement update, and NLOSMA will be applied between them. The filter needs to be initialized using a single-epoch LSR method. In the system propagation step, the state consisting of the antenna position and the receiver clock offset is predicted based on the system model. NLOSMA then utilizes the measured pseudo-ranges and the predicted position, which serves as the approximate solution, to calculate the corresponding pseudo-range corrections. Afterwards, in the measurement update step, the EKF uses the corrected measurements to update the state vector and its covariance.

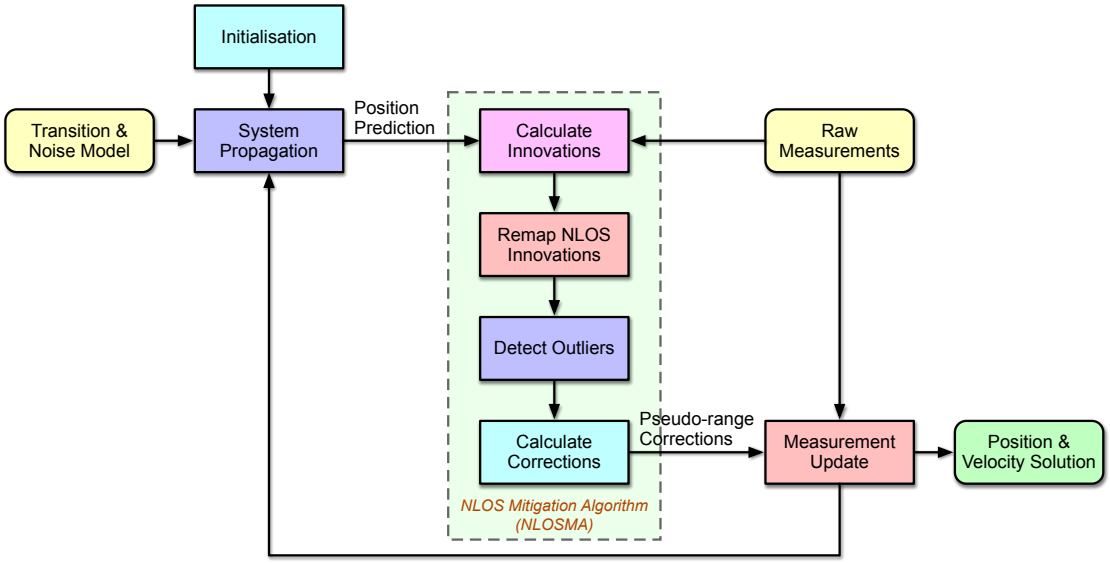

Figure 3: Components of the least-squares ranging with NLOS mitigation algorithm

IV. EXPERIMENTS

IV.1. Experimental Setup

The test dataset consists of 13 three-minute GNSS records from the four major constellations of GPS, GLONASS, Galileo, and Beidou. They were collected at various locations in London Borough of Camden in October 2022 using a u-blox ZED-F9P GNSS receiver at a recording frequency of 1 Hz. The antenna was maintained at a height of 1.2 metres above the ground. The relative distances from the antenna to nearby landmarks were measured by a laser rangefinder, and the coordinates of the true

positions were subsequently extracted from the Ordnance Survey MasterMap in the form of east and north on the OSGB36 datum. The true classification of LOS and NLOS signals can be obtained in 2 steps using a 3D city model at the true positions. First, with the 3D mapping data at the true position, the maximum elevation of all buildings within a certain range at the azimuth where the satellite is located can be calculated, which is also the minimum elevation of the satellite that allows the user to receive its signal directly in that direction. The satellite elevation is then compared to this minimum visible elevation in order to classify the signal as LOS or NLOS.

The experimental locations are marked in Figure 4. At each test site, there are two sets of data, collected in the morning and afternoon, which gives the satellites enough time to orbit to significantly different positions, enabling the morning and afternoon data to be independent of each other. Therefore, the afternoon dataset is used for tuning the configurable parameters of the positioning and filtering algorithms, while the morning one is used for testing.

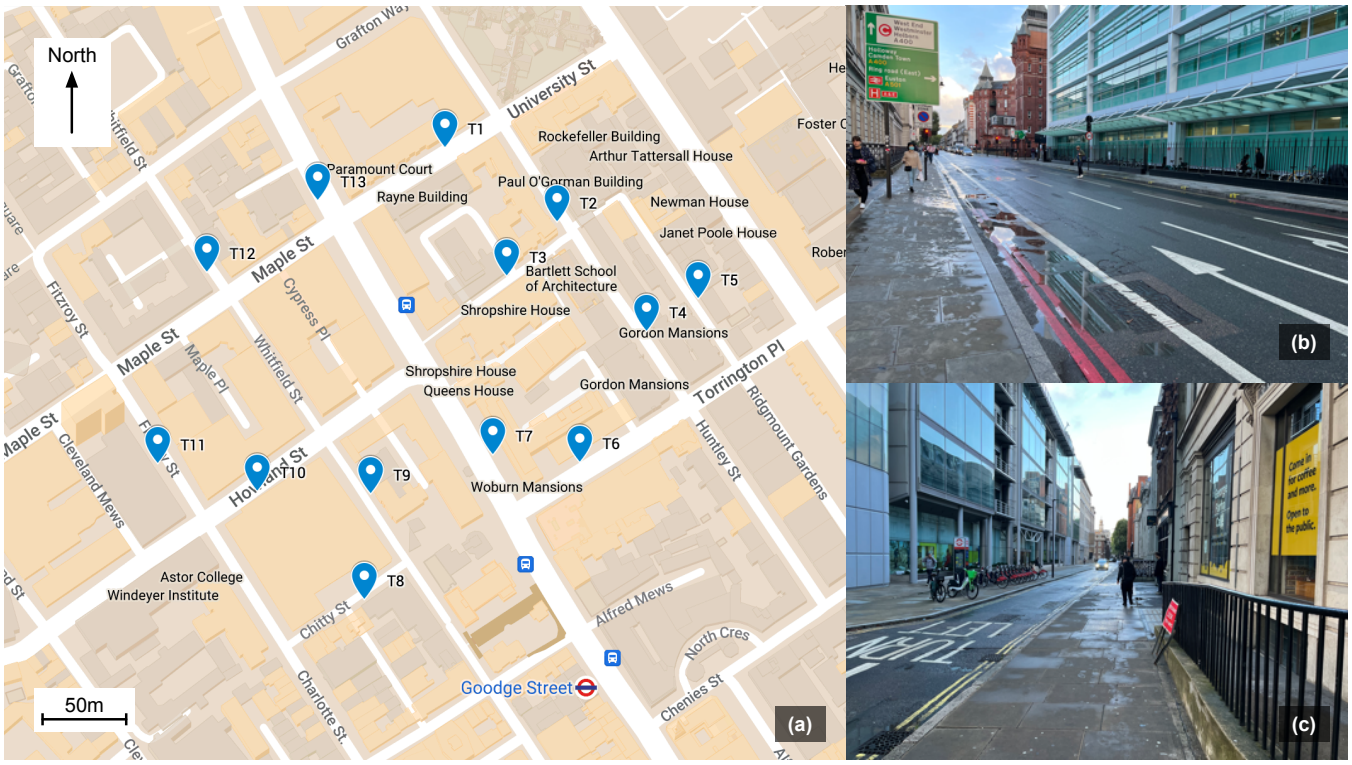

Figure 4: (a) True positions in London Borough of Camden (Background map ©Google Maps); (b) and (c) Example photos of the test environment

To validate the effectiveness of the proposed NLOS mitigation algorithm, the following algorithms were implemented, tested, and compared:

- LSR: Single-epoch least-squares ranging with terrain height aiding
- LSR NLOSMA: Single-epoch least-squares ranging with terrain height aiding and the NLOS mitigation algorithm
- LBR: Single-epoch likelihood-based ranging using 3D mapping data
- EKF: Multi-epoch extended Kalman filtering with terrain height aiding
- EKF NLOSMA: Multi-epoch extended Kalman filtering with terrain height aiding and the NLOS mitigation algorithm

The LBR algorithm, which utilizes 3D mapping data as additional information, serves as the benchmark for comparison with the NLOSMA proposed in this paper. A comprehensive description of its implementation can be found in (Groves et al., 2020; Zhong and Groves, 2022b).

Table 1: Experimental information (training data)

ID	No. of epochs	True position coordinates, m (Easting, Northing)	$\bar{n}_{sat}$	$\bar{n}_{NLOS}$	μ_{C/N_0}, dB-Hz	σ_{C/N_0}, dB-Hz	μ_{elev}, degrees	σ_{elev}, degrees
T1	180	(529430.28, 182145.56)	27.8	13.7	34.1	9.2	38.3	21.1
T2	180	(529498.19, 182103.04)	28.9	13.4	32.7	8.4	38.2	21.6
T3	180	(529468.86, 182070.56)	28.6	12.5	33.5	9.0	39.0	20.8
T4	180	(529552.67, 182040.07)	26.7	12.0	34.1	9.6	40.3	21.1
T5	180	(529582.42, 182060.45)	23.8	9.6	34.8	9.8	42.4	21.1
T6	180	(529515.04, 181961.61)	24.0	10.8	33.8	9.5	43.2	21.2
T7	180	(529463.37, 181965.37)	28.9	10.6	34.7	8.9	38.4	22.6
T8	180	(529390.02, 181877.45)	24.9	16.1	32.5	9.9	41.5	22.2
T9	180	(529391.58, 181939.90)	25.2	10.9	34.5	9.4	42.6	21.8
T10	180	(529325.19, 181939.89)	31.7	16.7	32.6	8.6	34.7	23.7
T11	180	(529265.69, 181954.87)	29.5	14.3	32.5	8.4	36.3	23.6
T12	180	(529291.57, 182068.25)	26.4	13.7	34.1	9.7	38.7	23.0
T13	180	(529356.04, 182112.39)	27.4	13.2	35.4	9.1	39.6	23.6

IV.2. Data Presentation and Parameter Determination

Table 1 presents a summary of the experimental data, including the number of epochs per segment, the true position expressed in projected coordinates on the OSGB36 datum, and the observational statistics. These statistics include the average number of satellites observed per epoch $\bar{n}_{sat}$, the average number of NLOS signals per epoch $\bar{n}_{NLOS}$ (determined by the 3D mapping data at the true positions), the mean and standard deviation of the C/N_0 represented as μ_{C/N_0} and σ_{C/N_0}, respectively, and the mean and standard deviation of the elevation represented as μ_{elev} and σ_{elev}, respectively.

The C/N_0 and elevation values are usually thought to be important criteria for classifying LOS and NLOS signals. Generally, a larger C/N_0 value and higher elevation angle indicate a greater probability of an LOS signal. Figure 5 shows their distributions for LOS and NLOS signals at true positions. The figure shows that the distribution of C/N_0 seems to be more discriminative than that of elevation for distinguishing between LOS and NLOS signals. As seen in the left panel of Figure 5, a threshold of 40 dB-Hz appears to be a suitable cutoff point above which signals are more likely to be LOS, and below which they are more likely to be NLOS. In the elevation plot, however, while the number of LOS signals dominates when the elevation is above 70 degrees, it is difficult to distinguish between LOS and NLOS signals for the remaining angles.

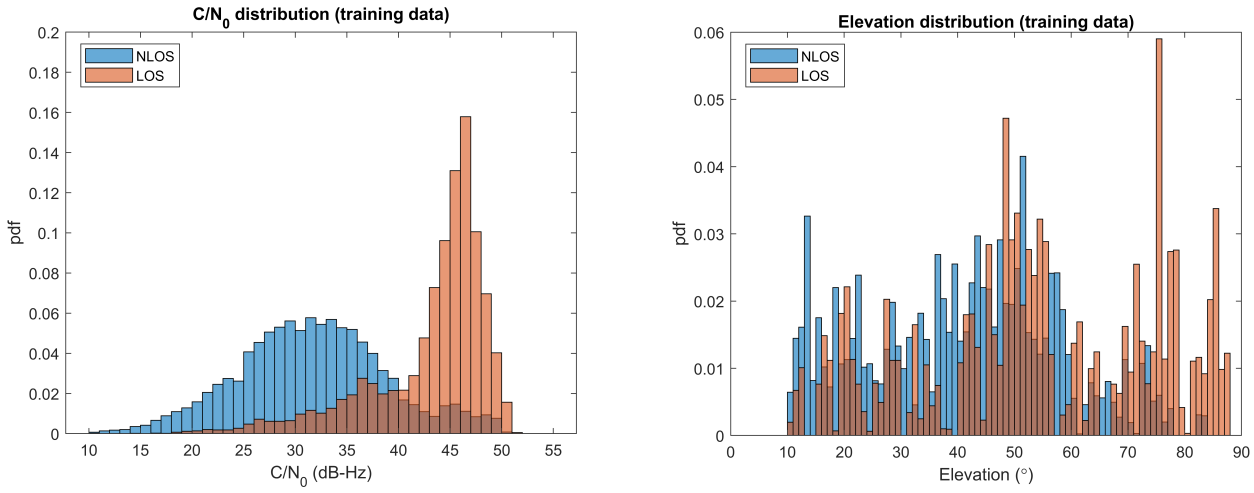

Figure 5: C/N_0 and elevation distributions at true positions

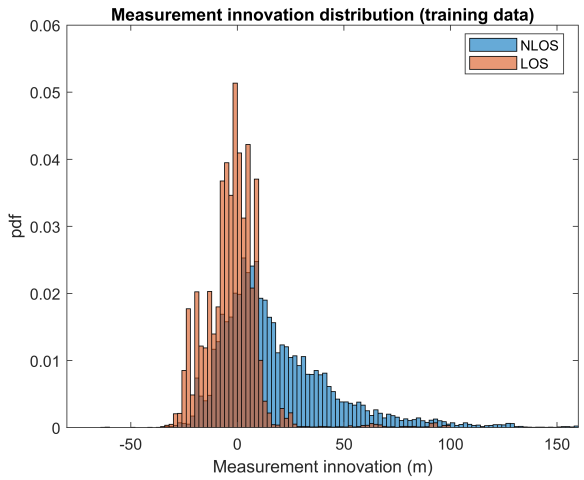

Figure 6: Measurement innovation distribution at true positions

At true positions, the measured pseudo-range is corrected for any known errors other than the NLOS path delay. The measurement innovation is computed by subtracting the corresponding satellite-to-receiver distance from the corrected pseudo-range. The LOS satellite with the strongest signal strength is then selected as the reference satellite, followed by the measurement innovation being differenced with respect to the reference satellite to remove the receiver clock offset. Figure 6 shows the measurement innovation distributions for LOS and NLOS signals at true positions. It is apparent that the innovations of the LOS signal are primarily distributed around 0 and generally conform to a normal distribution, while the innovations of the NLOS signal clearly deviate from a normal distribution and exhibit a long tail with a mean value significantly larger than 0.

Equation (3) relates the C/N_0 value of the LOS signal to the variance of the measurement innovation, and Figure 7 illustrates their relationship using the training data. As shown in the figure, as the C/N_0 value of the signal increases, the variance of its corresponding measurement innovation decreases. The variance of the reference satellite, σ_r^2, is estimated together with the LOS variance estimation. The values of the parameters in Equation (3) are given in Table 2 by fitting the data points in the figure.

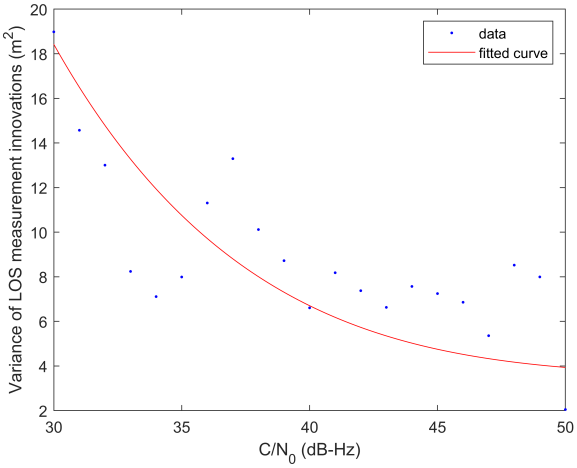

Figure 7: Relationship between the variance of LOS measurement innovations and C/N_0 values

Once the mean and variance of the measurement innovations for LOS signals are obtained, the mean and variance of the NLOS path delay in Equations (4) to (6) can be calculated over a series of C/N_0 intervals and then weighted to average. Large measurement innovation errors are preferentially corrected. Specifically, the higher the deviation of the measurement innovation, the greater the weight it receives. This approach minimises the impact of large measurement deviations on the

positioning performance.

The values of all parameters in NLOSMA are summarised in Table 2.

Table 2: Parameters used in the NLOS mitigation algorithm (NLOSMA)

a, m^2	$b + \sigma_r^2, m^2$	μ_{LOS}, m	μ_{NLOS}, m	σ_{NLOS}, m	T_{C/N_0}, dB-Hz	T_{δ_z}
3.272×10^5	12.23	0	31	212	40	4.24

IV.3. Experimental Results

Figure 8 shows the root mean square (RMS) errors of the horizontal position solutions obtained from the dataset collected at 13 experimental sites in London. Because all the algorithms involved in the tests included terrain height aiding techniques, only errors in the horizontal radial direction were assessed. As shown in Figure 8, the first three bars from the left represent the single-epoch positioning results obtained using LSR (least-squares ranging), LSR with NLOSMA (non-line-of-sight mitigation algorithm) and 3DMA (3D-mapping aided) LBR (likelihood-based ranging), respectively. The last two bars show the multi-epoch positioning results obtained using EKF (extended Kalman filtering) with and without NLOSMA, respectively. Detailed results are presented in Tables 3 to 5 and Figures 10 to 22 in Appendix B.

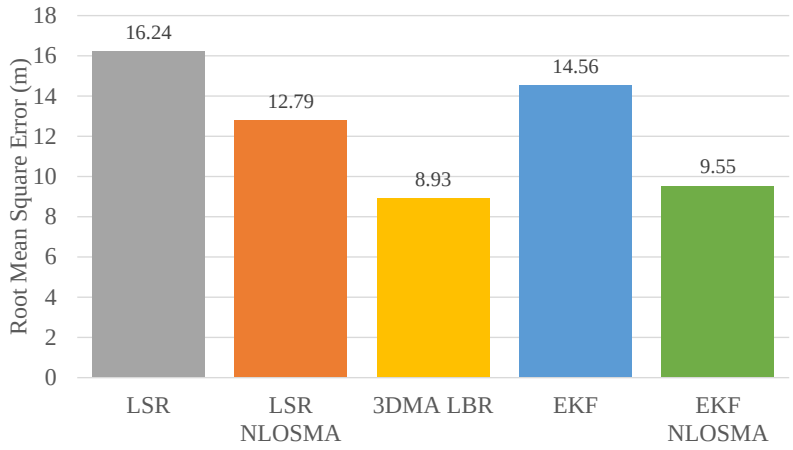

Figure 8: Horizontal radial position root mean square (RMS) error

In the case of single-epoch positioning, Figure 8 shows that the RMS error of the LSR solution is 16.24 m, which is higher than the other two single-epoch methods involved in the test. The error in the results calculated by LSR with NLOSMA was approximately 12.8 m, representing a reduction of approximately 21% in the RMS error of the solution compared to the conventional LSR algorithm. As can be seen from Table 3 in Appendix B, the LSR with NLOSMA shows varying degrees of improvement in RMS error compared to the one without NLOSMA in 11 of the 13 test sites, reaching up to about 52% (as in Test Site T4). At the epoch level, NLOSMA shows an improvement in about 72% of the epochs, which clearly demonstrates that the NLOSMA proposed in this paper has a positive effect on urban localization.

To further illustrate the effectiveness of the NLOSMA in mitigating NLOS errors, Figure 9 consists of two plots displaying the error distribution of measurement innovations over true positions before and after the application of the NLOSMA. As shown in the left plot of Figure 9, the error distribution of the original measurement innovations follows the expected pattern, with the error distribution of the LOS signals closely approximating a normal distribution, while that of the NLOS signals clearly deviating from a normal distribution. After applying the NLOSMA, it can be seen from the right plot of Figure 9 that the measurement innovation error distribution for NLOS signals is much closer to a normal distribution compared to the original data. It needs be noted that this improvement comes with a small increase in the variance of the errors of the LOS and NLOS signals. Additionally, it is also observed that there are cases where the NLOSMA misclassifies or improperly corrects some pseudo-range measurements, resulting in a degradation in performance rather than an improvement.

However, without additional information, it can be challenging to accurately distinguish between LOS and NLOS signals based on available information such as signal strength and elevation angle. As demonstrated in Figure 8, with the aid of 3D mapping

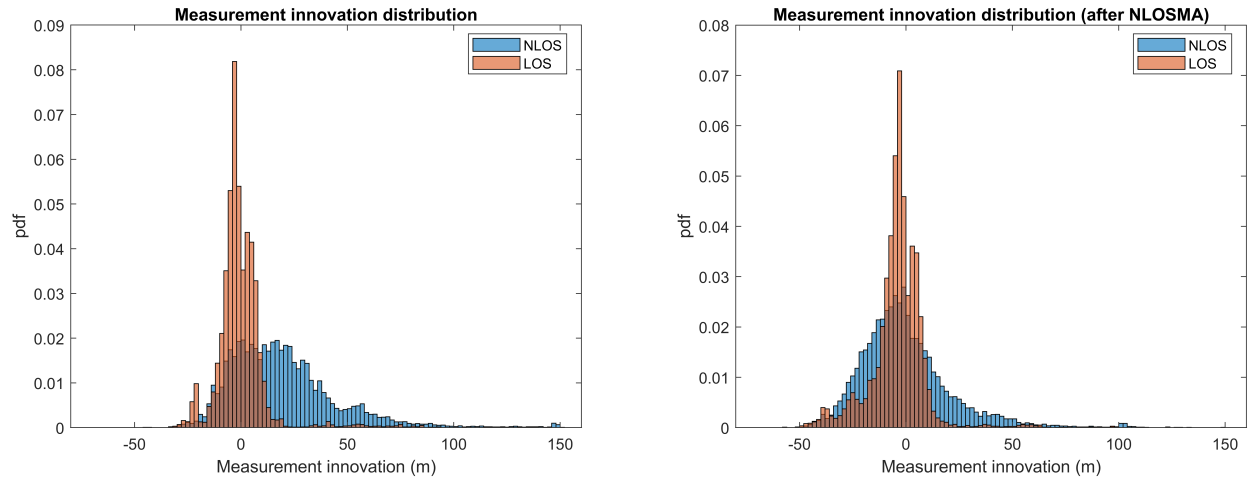

Figure 9: Comparison between the measurement innovation distributions at true positions

data, the positioning error of the single-epoch 3DMA LBR is further reduced to around 9 m, representing a 45% and 30% improvement compared to LSR without and with NLOSMA, respectively. The performance of 3DMA LBR is not always superior to the other two single-epoch algorithms, as seen in Appendix B Table 3. In some cases, 3DMA LBR may encounter ambiguity problems and deviate from the correct position, or even give completely incorrect position solutions (as in Test Site T5), resulting in larger errors than the other methods.

In multi-epoch positioning, since all tests are static positioning, the performance of the conventional EKF is not significantly improved compared to the single-epoch conventional LSR results. Because for static positioning, NLOS and multipath errors are largely correlated over successive epochs, making them difficult to mitigate by the filtering process. NLOSMA improved the positioning results more in the multi-epoch positioning than in the single-epoch case. Figure 8 shows that the NLOSMA-equipped EKF improves the position solution by more than one-third compared to the conventional EKF. This is probably because the filtering attenuates the noise-like errors and mitigates the impact of incorrect position solutions caused by NLOSMA providing incorrect measurement corrections due to C/N_0 and pseudo-range fluctuations.

It is important to note that the performance of NLOSMA can be affected by the accuracy of the classification of LOS and NLOS signals. Because the algorithm relies on being able to accurately distinguish between LOS and NLOS signals in order to apply the appropriate corrections. NLOSMA can fail completely due to the inability of the LOS/NLOS classifier to provide accurate predictions. Factors such as signal strength and elevation angle can all play a role in the classification process. However, after observing and testing the distribution of C/N_0 and elevation angles, C/N_0 was finally chosen as the only criterion for LOS/NLOS determination in this paper.

Additionally, the processing of the classified signals can also impact the performance of NLOSMA. Since the classification of LOS and NLOS signals cannot be perfectly accurate, the processing of the classified signals should take into account not only the correctly classified signals, but also the misclassified ones. It is a trade-off between the improvement resulting from the correction of the correctly classified signal and the additional error resulting from the correction of the misclassified signal. One possible implementation is to estimate the probability of the NLOS of the signal and then multiply it with its pseudo-range correction, which allows effective interpolation between LOS- and NLOS-hypothesis measurements based on the NLOS probability.

In terms of computational efficiency, NLOSMA places little burden on the original positioning algorithm as all of its calculations can be done in batch without the use of loops. Compared to candidate position-based hypothesis testing algorithms, it only needs to be computed at a single approximate position, which significantly reduces the amount of computation. In contrast to methods that require additional information, it does not need to process additional information and thus does not incur additional computational load.

V. CONCLUSIONS

Multipath effects and NLOS reception occur frequently in urban environments. The results of experiments conducted in London confirm that the distribution of measurement innovation errors does not conform to a normal distribution. This deviation in the error distribution invalidates the assumption that errors are normally distributed in conventional GNSS positioning methods,

which can negatively impact GNSS positioning performance in urban areas.

The NLOS mitigation algorithm (NLOSMA) proposed in this paper utilizes the measured C/N_0 values to classify the received signals into LOS and NLOS and maps their measurement innovation errors into symmetric and asymmetric distributions, respectively. The algorithm then employs a cumulative distribution function (CDF) to relate these two distributions and calculates the compensation value for pseudo-range measurements. A comparison of the error distribution of measurement innovations before and after the implementation of NLOSMA reveals that NLOSMA can effectively improve the error distribution of NLOS signals.

The experimental results show that the implementation of NLOSMA can improve the positioning performance of conventional GNSS in urban environments without the need for additional information and without a significant reduction in computational efficiency. Specifically, it results in an improvement of approximately 21% and 34% in the RMS horizontal position error compared to the conventional LSR and EKF algorithms for single- and multi-epoch positioning, respectively.

VI. FUTURE WORK

The current version of the NLOS mitigation algorithms for GNSS positioning is still in its early stages and has much room for improvement. Areas worth exploring further include:

- Kinematic positioning test.

  In this paper, the effectiveness of NLOSMA has been tested in static positioning, whereas in reality pedestrians and vehicles are usually in motion. Therefore, NLOSMA needs further proof of its effectiveness in tests with pedestrians and vehicles in motion.

- More accurate classification of LOS and NLOS signals.

  The ability to accurately classify LOS and NLOS signals is key to the effectiveness of NLOSMA. Those misclassified signals can introduce unexpected errors. The authors tried C/N_0, elevation, and a combination of them as criteria to distinguish between LOS and NLOS signals. However, Figure 5 suggests that using C/N_0 alone produced the best results. Other potential factors, such as the rate of the measurement innovation error, deserve to be explored further.

- Modelling pseudo-range innovations using other asymmetric distributions.

  Due to time constraints, only one asymmetric distribution is demonstrated in this paper. The skew-normal distribution was chosen for two main reasons. First, as shown in Figure 6, the NLOS pseudo-range innovation distribution looks like a skew-normal distribution. Second, it is closely related to the normal distribution and can be easily remapped into the normal distribution. Asymmetric distributions other than the skew-normal distribution can also be attempted in future studies.

ACKNOWLEDGEMENTS

Qiming Zhong is funded by the China Scholarship Council and a UCL Engineering Faculty Scholarship. The author thanks his PhD supervisor, Dr. Paul Groves, whose comments have greatly improved the quality of the manuscript.

REFERENCES

Biagi, L. and Caldera, S. (2013). An Efficient Leave One Block Out approach to identify outliers. *Journal of Applied Geodesy*, 7(1):11–19.

Egea-Roca, D., Tripiana-Caballero, A., López-Salcedo, J. A., Seco-Granados, G., Wilde, W. D., Bougard, B., Sleewaegen, J. M., and Popugaev, A. (2018). GNSS Measurement Exclusion and Weighting with a Dual Polarized Antenna: The FANTASTIC project. *ICL-GNSS 2018 - 2018 8th International Conference on Localization and GNSS: Seamless Indoor-Outdoor Localization, Proceedings*.

European GNSS Agency (2018). *GNSS user technology report. Issue 2*. Publications Office of the European Union. `https://data.europa.eu/doi/10.2878/743965`.

Gentner, C., Ulmschneider, M., Kuehner, I., and Dammann, A. (2020). WiFi-RTT Indoor Positioning. In *2020 IEEE/ION Position, Location and Navigation Symposium (PLANS)*, pages 1029–1035. IEEE.

Groves, P. D. (2013). *Principles of GNSS, inertial, and multisensor integrated navigation systems*. Artech House, Boston; London.

Groves, P. D. and Jiang, Z. (2013). Height aiding, C/N0 weighting and consistency checking for GNSS NLOS and multipath mitigation in urban areas. *Journal of Navigation*, 66(5):653–669.

Groves, P. D., Jiang, Z., Rudi, M., and Strode, P. (2013). A portfolio approach to NLOS and multipath mitigation in dense urban areas. *26th International Technical Meeting of the Satellite Division of the Institute of Navigation, ION GNSS 2013*, 4(September):3231–3247.

Groves, P. D., Zhong, Q., Faragher, R., and Esteves, P. (2020). Combining inertially-aided extended coherent integration (Supercorrelation) with 3D-mapping-aided GNSS. In *Proceedings of the 33rd International Technical Meeting of the Satellite Division of the Institute of Navigation, ION GNSS+ 2020*, pages 2327–2346. Institute of Navigation (ION).

Hsu, L. T. (2017). GNSS multipath detection using a machine learning approach. *2017 IEEE 20th International Conference on Intelligent Transportation Systems (ITSC)*, pages 1–6.

Hsu, L. T., Gu, Y., and Kamijo, S. (2015a). NLOS correction/exclusion for GNSS measurement using RAIM and city building models. *Sensors (Switzerland)*, 15(7):17329–17349.

Hsu, L. T., Gu, Y., and Kamijo, S. (2016). 3D building model-based pedestrian positioning method using GPS/GLONASS/QZSS and its reliability calculation. *GPS Solutions*, 20(3):413–428.

Hsu, L. T., Jan, S. S., Groves, P. D., and Kubo, N. (2015b). Multipath mitigation and NLOS detection using vector tracking in urban environments. *GPS Solutions*, 19(2):249–262.

Hsu, L. T., Tokura, H., Kubo, N., Gu, Y., and Kamijo, S. (2017). Multiple Faulty GNSS Measurement Exclusion Based on Consistency Check in Urban Canyons. *IEEE Sensors Journal*, 17:1909–1917.

Jiang, Z. and Groves, P. D. (2014). NLOS GPS signal detection using a dual-polarisation antenna. *GPS Solutions*, 18:15–26.

Kaplan, E. D. and Hegarty, C. (2017). *Understanding GPS/GNSS: Principles and Applications*. Artech House, 3 edition.

Keshvadi, M., Broumandan, A., and Lachapelle, G. (2011). Analysis of GNSS Beamforming and Angle of Arrival Estimation in Multipath Environments. *Proceedings of the 2011 International Technical Meeting of The Institute of Navigation*, pages 427–435.

Lyu, Z. and Gao, Y. (2020). An SVM Based Weight Scheme for Improving Kinematic GNSS Positioning Accuracy with Low-Cost GNSS Receiver in Urban Environments. *Sensors*, 20.

Lyu, Z. and Gao, Y. (2020). A New Method for Non-line-of-sight GNSS Signal Detection for Positioning Accuracy Improvement in Urban Environments. *Proceedings of the 33rd International Technical Meeting of the Satellite Division of The Institute of Navigation (ION GNSS+ 2020)*, pages 2972–2988.

Marais, J., Meurie, C., Attia, D., Ruichek, Y., and Flancquart, A. (2014). Toward accurate localization in guided transport: Combining GNSS data and imaging information. *Transportation Research Part C: Emerging Technologies*, 43:188–197.

McGraw, G. A., Groves, P. D., and Ashman, B. W. (2020). *Robust Positioning in the Presence of Multipath and NLOS GNSS Signals*, chapter 22, pages 551–589. John Wiley & Sons, Ltd.

Meguro, J. I., Murata, T., Takiguchi, J. I., Amano, Y., and Hashizume, T. (2009). GPS multipath mitigation for urban area using omnidirectional infrared camera. *IEEE Transactions on Intelligent Transportation Systems*, 10:22–30.

Misra, P. and Enge, P. (2010). *Global positioning system : signals, measurements, and performance*. Ganga-Jamuna Press.

Miura, S., Hsu, L. T., Chen, F., and Kamijo, S. (2015). GPS Error Correction With Pseudorange Evaluation Using Three-Dimensional Maps. *IEEE Transactions on Intelligent Transportation Systems*, 16:3104–3115.

Ng, H. F., Zhang, G., and Hsu, L. T. (2020). A Computation Effective Range-Based 3D Mapping Aided GNSS with NLOS Correction Method. *Journal of Navigation*, 73(6):1202–1222.

Ng, H. F., Zhang, G., and Hsu, L. T. (2021). Robust GNSS Shadow Matching for Smartphones in Urban Canyons. *IEEE Sensors Journal*, 21(16):18307–18317.

Sun, R., Wang, G., Zhang, W., Hsu, L. T., and Ochieng, W. (2019). A gradient boosting decision tree based GPS signal reception classification algorithm. *Applied Soft Computing*, 86:105942.

Suzuki, T. (2016). Integration of GNSS positioning and 3D map using particle filter. *29th International Technical Meeting of the Satellite Division of the Institute of Navigation, ION GNSS 2016*, 2:1296–1304.

Suzuki, T. and Kubo, N. (2013). Correcting GNSS multipath errors using a 3D surface model and particle filter. *26th International Technical Meeting of the Satellite Division of the Institute of Navigation, ION GNSS 2013*, 2:1583–1595.

Usman, M., Asghar, M. R., Ansari, I. S., Granelli, F., and Qaraqe, K. A. (2018). Technologies and Solutions for Location-Based Services in Smart Cities: Past, Present, and Future. *IEEE Access*, 6:22240–22248.

Vagle, N., Broumandan, A., and Lachapelle, G. (2017). Multi-antenna GNSS and INS/Odometer Coupling for Robust Vehicular Navigation. In *ENAC*.

van Diggelen, F. (2021). Google's Use of 3D Building Models to Solve Urban GNSS. `https://www.ion.org/itm/abstracts.cfm?paperID=10048`.

Wang, H., Pan, S., Gao, W., Xia, Y., and Ma, C. (2022). Multipath/NLOS Detection Based on K-Means Clustering for GNSS/INS Tightly Coupled System in Urban Areas. *Micromachines*, 13:1128.

Wang, L. (2015). *Investigation of Shadow Matching for GNSS Positioning in Urban Canyons*. PhD thesis, University College London.

Wang, L., Groves, P. D., and Ziebart, M. K. (2015). Smartphone shadow matching for better cross-street GNSS positioning in urban environments. *Journal of Navigation*, 68(3):411–433.

Ward, P. W., Betz, J. W., and Hegarty, C. J. (2017). *GNSS Disruptions*, chapter 9, pages 549–617. Artech House, 3 edition.

Wen, W. and Hsu, L. T. (2022). 3D LiDAR Aided GNSS NLOS Mitigation in Urban Canyons. *IEEE Transactions on Intelligent Transportation Systems*, 23:18224–18236.

Wen, W., Zhang, G., and Hsu, L. T. (2021). GNSS NLOS Exclusion Based on Dynamic Object Detection Using LiDAR Point Cloud. *IEEE Transactions on Intelligent Transportation Systems*, 22:853–862.

Yozevitch, R., Moshe, B. B., and Weissman, A. (2016). A Robust GNSS LOS/NLOS Signal Classifier. *NAVIGATION*, 63:429–442.

Yuan, Y., Shen, F., and Li, X. (2020). GPS multipath and NLOS mitigation for relative positioning in urban environments. *Aerospace Science and Technology*, 107:106315.

Zhang, G., Wen, W., Xu, B., and Hsu, L. T. (2020). Extending Shadow Matching to Tightly-Coupled GNSS/INS Integration System. *IEEE Transactions on Vehicular Technology*, 69(5):4979–4991.

Zhong, Q. and Groves, P. (2022a). Outlier Detection for 3D-Mapping-Aided GNSS Positioning. *Proceedings of the 35th International Technical Meeting of the Satellite Division of The Institute of Navigation (ION GNSS+ 2022)*, pages 2104–2126.

Zhong, Q. and Groves, P. D. (2022b). Multi-Epoch 3D-Mapping-Aided Positioning using Bayesian Filtering Techniques. *NAVIGATION: Journal of the Institute of Navigation*, 69(2).

Zidan, J., Adegoke, E. I., Kampert, E., Birrell, S. A., Ford, C. R., and Higgins, M. D. (2021). GNSS Vulnerabilities and Existing Solutions: A Review of the Literature. *IEEE Access*, 9:153960–153976.

Ziedan, N. I. (2017). Urban positioning accuracy enhancement utilizing 3D buildings model and accelerated ray tracing algorithm. *30th International Technical Meeting of the Satellite Division of the Institute of Navigation, ION GNSS 2017*, 5:3253–3268.

Ziedan, N. I. (2019). Enhancing GNSS mobile positioning in urban environments through utilization of multipath prediction and consistency analysis. *Proceedings of the 32nd International Technical Meeting of the Satellite Division of the Institute of Navigation, ION GNSS+ 2019*, pages 3469–3483.

APPENDIX A DETAILED DESCRIPTION OF ALGORITHMS

A.1 Least-Squares Ranging

A GNSS position solution can be calculated from a set of pseudo-range measurements using least-squares estimation, which is given by (Groves, 2013)

$$\mathbf{x}^{+} = \mathbf{x}^{-} + \left(\mathbf{H}^{\mathrm{T}}\mathbf{W}^{-1}\mathbf{H}\right)^{-1}\mathbf{H}^{\mathrm{T}}\mathbf{W}^{-1}\delta\mathbf{z} \tag{11}$$

where $\mathbf{x}^{+}$ and $\mathbf{x}^{-}$ are, respectively, the estimated and predicted state vectors, $\delta\mathbf{z}$ is the measurement innovation vector, $\mathbf{H}$ is the measurement matrix, and $\mathbf{W}$ is the weighting matrix.

The state vector in conventional GNSS positioning typically consists of the Cartesian Earth-centred Earth-fixed (ECEF) position of the receiver, $\mathbf{r}_a = [x_a, y_a, z_a]^{\mathrm{T}}$, and the receiver clock offset, $\delta\rho_c^a$, as shown in

$$\mathbf{x} = \begin{bmatrix} \mathbf{r}_a \\ \delta\rho_c^a \end{bmatrix} \tag{12}$$

The measurement innovation vector, $\delta\mathbf{z}$, is formulated by

$$\delta\mathbf{z} = \begin{bmatrix} \rho'_{1,C} - r_{a1} - \delta\rho_c^a \\ \rho'_{2,C} - r_{a2} - \delta\rho_c^a \\ \vdots \\ \rho'_{j,C} - r_{aj} - \delta\rho_c^a \end{bmatrix} \tag{13}$$

where $\rho'_{j,C}$ is the measured pseudo-ranges corrected for all known errors such as atmospheric delays, satellite clock offsets and inter-constellation clock offsets, and r_{aj} is the predicted range from the approximate user position, $\mathbf{r}_a$, to satellite j, given by

$$r_{aj} = \sqrt{\left[\mathbf{C}_e^I\left(r_{aj}\right)\mathbf{r}_j - \mathbf{r}_a\right]^{\mathrm{T}}\left[\mathbf{C}_e^I\left(r_{aj}\right)\mathbf{r}_j - \mathbf{r}_a\right]} \tag{14}$$

where $\mathbf{r}_j$ is the Cartesian ECEF position of the j^{th} satellite, and $\mathbf{C}_e^I$ is the Sagnac effect compensation matrix, given by

$$\mathbf{C}_e^I\left(r_{aj}\right) \approx \begin{bmatrix} 1 & \omega_{ie}r_{aj}/\,c & 0 \\ -\omega_{ie}r_{aj}/\,c & 1 & 0 \\ 0 & 0 & 1 \end{bmatrix} \tag{15}$$

where the Earth rotation rate, ω_{ie}, is 7.292115×10^{-5} rad/s, and the speed of light, c, is 299792458 m/s. The measurement matrix, $\mathbf{H}$, is formulated by

$$\mathbf{H} = \begin{bmatrix} -u_{1,x} & -u_{1,y} & -u_{1,z} & 1 \\ -u_{2,x} & -u_{2,y} & -u_{2,z} & 1 \\ \vdots & \vdots & \vdots & \vdots \\ -u_{j,x} & -u_{j,y} & -u_{j,z} & 1 \end{bmatrix} \tag{16}$$

where $\mathbf{u}_j = [u_{j,x}, u_{j,y}, u_{j,z}]^{\mathrm{T}}$ is the line-of-sight unit vector from the approximate user position, $\mathbf{r}_a$, to satellite j, given by

$$\mathbf{u}_j = \frac{\mathbf{C}_e^I\left(r_{aj}\right)\mathbf{r}_j - \mathbf{r}_a}{r_{aj}} \tag{17}$$

The weighting matrix, $\mathbf{W}$, is calculated by

$$\mathbf{W} = \begin{bmatrix} \sigma_1^2 & 0 & \cdots & 0 \\ 0 & \sigma_2^2 & \cdots & 0 \\ \vdots & \vdots & \ddots & \vdots \\ 0 & 0 & \cdots & \sigma_j^2 \end{bmatrix} \tag{18}$$

where σ_j^2 is the variance of the measurement innovation for satellite j, given by,

$$\sigma_j^2 = a \times 10^{-(C/N_0)_j/10} + b \tag{19}$$

where a and b are empirically determined constants.

A Leave One Out approach (Biagi and Caldera, 2013) is used for outlier detection and elimination in the least-squares ranging. This outlier detection and elimination method is exclusively applied to the conventional LSR, and omitted in the LSR with NLOSMA as it already incorporates an outlier detection module in NLOSMA. The observation vector is assumed to be composed of m completely uncorrelated elements, and the number of unknowns in the state vector is $n = 4$. Assuming that there is an outlier in the measurements, the solution calculated from the remaining observations is used to estimate the suspected outlier. The residual between this estimated value and the measured value is then fed to a hypothesis test of an F distribution with 1 degree of freedom in the numerator and $m - n - 1$ degrees of freedom in the denominator. The confidence level is set to 0.99. Where all measurements pass the F-tests, the position solution is accepted. Otherwise, the measurement with the largest residual is then eliminated as it is least consistent with the others and a new least-squares solution is then calculated. The process repeats until either all observations pass the hypothesis tests or only 4 measurements remain.

To apply the terrain height aid, a virtual satellite can be assumed at the centre of the Earth and used as the $(j+1)^{th}$ measurement. Therefore, the measurement innovation vector, $\delta\mathbf{z}$, is appended with the difference between the terrain height and the current position estimate.

$$\delta\mathbf{z}_{j+1} = r_{ter} - |\mathbf{r}_a| \tag{20}$$

where r_{ter} consists of the radius of the Earth, the terrain height (obtained from the mapping data) and the antenna height above the ground. The line-of-sight unit vector from the receiver to this virtual satellite is

$$\mathbf{u}_{j+1} = \mathbf{u}_a \approx \frac{\mathbf{r}_a}{|\mathbf{r}_a|} \tag{21}$$

The $(j+1)^{th}$ row it occupies in the measurement matrix, $\mathbf{H}$, is

$$\mathbf{H}_{j+1} = [u_{a,x} \quad u_{a,y} \quad u_{a,z} \quad 0] \tag{22}$$

The corresponding variance of the height-aiding measurement, which constitutes the $(j+1)^{th}$ diagonal element of $\mathbf{W}$, is assumed to be equivalent to that of the satellite with the highest C/N_0 value in the epoch for the results presented in this paper.

A.2 Extended Kalman Filtering

As it is static positioning, the state vector in Epoch k consists of the ECEF position of the receiver, $\mathbf{r}_{a,k} = [x_{a,k}, y_{a,k}, z_{a,k}]^{\mathrm{T}}$, and the receiver clock offset, $\delta\rho_{c,k}^a$, as shown in

$$\mathbf{x}_k = \begin{bmatrix} \mathbf{r}_{a,k} \\ \delta\rho_{c,k}^a \end{bmatrix} \tag{23}$$

The initial state is calculated by the least-squares ranging. The Kalman filter includes prediction and update steps. In the propagation step, the position state estimates remain unchanged due to static positioning, while the error covariance increases. Hence, the transition matrix, $\mathbf{\Phi}_{k-1}$, is an identity matrix, given by

$$\mathbf{\Phi}_{k-1} = \mathbf{I}_4 = \begin{bmatrix} 1 & 0 & 0 & 0 \\ 0 & 1 & 0 & 0 \\ 0 & 0 & 1 & 0 \\ 0 & 0 & 0 & 1 \end{bmatrix} \tag{24}$$

The corresponding system noise covariance matrix is given by

$$\mathbf{Q}_{k-1} = \begin{bmatrix} \frac{1}{3}S_a\tau_s^3\mathbf{I}_3 & \mathbf{0}_{3\times1} \\ \mathbf{0}_{1\times3} & S_{cf}\tau_s \end{bmatrix} \tag{25}$$

where $\mathbf{I}_n$ is a $n \times n$ identity matrix, $\mathbf{S}_a$ is the acceleration power spectral density (PSD), S_{cf} is the receiver clock frequency drift PSD, and τ_s is the time interval between epochs.

The state estimate and its error covariance matrix are propagated by

$$\mathbf{x}_k^- = \mathbf{\Phi}_{k-1}\mathbf{x}_{k-1}^+ \tag{26}$$

$$\mathbf{P}_k^- = \mathbf{\Phi}_{k-1}\mathbf{P}_{k-1}^+\mathbf{\Phi}_{k-1}^{\mathrm{T}} + \mathbf{Q}_{k-1} \tag{27}$$

where the superscripts $^-$ and $^+$ indicate estimation and update, respectively.

In the measurement update step, the measurement noise covariance, $\mathbf{R}_k$, is then obtained using

$$\mathbf{R}_k = \begin{bmatrix} \sigma_{1,k}^2 & 0 & \cdots & 0 \\ 0 & \sigma_{2,k}^2 & \cdots & 0 \\ \vdots & \vdots & \ddots & \vdots \\ 0 & 0 & \cdots & \sigma_{j,k}^2 \end{bmatrix} \tag{28}$$

where σ_j is calculated in the same way as in Equation (19). The measurement matrix, $\mathbf{H}_k$, is given by

$$\mathbf{H}_k = \begin{bmatrix} -u_{1,k,x} & -u_{1,k,y} & -u_{1,k,z} & 1 \\ -u_{2,k,x} & -u_{2,k,y} & -u_{2,k,z} & 1 \\ \vdots & \vdots & \vdots & \vdots \\ -u_{j,k,x} & -u_{j,k,y} & -u_{j,k,z} & 1 \end{bmatrix} \tag{29}$$

where $\mathbf{u}_{j,k}$ is the line-of-sight unit vector of satellite j, given by Equation (17).

The measurement innovation, $\delta\mathbf{z}_k^-$, is computed using

$$\delta\mathbf{z}_k^- = \begin{bmatrix} \rho'_{1,C,k} - r_{a1,k} - \delta\rho_{c,k}^a \\ \rho'_{2,C,k} - r_{a2,k} - \delta\rho_{c,k}^a \\ \vdots \\ \rho'_{j,C,k} - r_{aj,k} - \delta\rho_{c,k}^a \end{bmatrix} \tag{30}$$

where $\rho'_{j,C,k}$ are the measured pseudo-ranges corrected for all known errors, and $r_{aj,k}$ is the predicted range from the approximate user position to satellite j.

The terrain height aiding applied here is similar to the one used in the least-squares ranging shown in Equations (20) to (22).

The Kalman gain is then computed using

$$\mathbf{K}_k = \mathbf{P}_k^-{\mathbf{H}_k}^{\mathrm{T}}\left(\mathbf{H}_k\mathbf{P}_k^-{\mathbf{H}_k}^{\mathrm{T}} + \mathbf{R}_k\right)^{-1} \tag{31}$$

The state estimate and the corresponding covariance are then updated using

$$\mathbf{x}_k^+ = \mathbf{x}_k^- + \mathbf{K}_k\delta\mathbf{z}_k^- \tag{32}$$

$$\mathbf{P}_k^+ = \left(\mathbf{I} - \mathbf{K}_k\mathbf{H}_k\right)\mathbf{P}_k^- \tag{33}$$

APPENDIX B DETAILED EXPERIMENTAL RESULTS

Table 3: Horizontal radial position RMS errors (in metres)

Test site	Algorithm				
	LSR	LSR NLOSMA	LBR	EKF	EKF NLOSMA
T1	18.13	11.81	6.01	12.50	6.41
T2	7.17	10.84	8.42	4.30	14.63
T3	13.45	10.14	6.23	8.81	14.52
T4	18.53	8.83	5.92	19.51	5.61
T5	8.95	8.61	21.99	9.79	10.99
T6	9.18	6.32	3.66	6.91	4.76
T7	29.36	21.77	9.87	23.71	5.57
T8	27.81	24.99	7.02	28.12	17.52
T9	14.85	10.28	7.33	14.07	4.56
T10	10.25	10.11	5.23	9.24	8.95
T11	9.37	12.09	8.40	7.96	5.19
T12	12.11	6.34	6.46	9.23	3.03
T13	12.85	9.15	4.39	13.92	8.32

Table 4: Maximum horizontal radial position error (in metres) at 90% confidence level

Test site	Algorithm				
	LSR	LSR NLOSMA	LBR	EKF	EKF NLOSMA
T1	25.04	16.19	7.53	13.35	7.85
T2	11.25	16.00	11.93	5.71	16.40
T3	19.25	15.27	9.20	9.76	16.19
T4	25.24	13.33	6.95	21.22	6.68
T5	12.55	11.77	31.19	11.78	12.94
T6	11.70	8.55	5.11	8.16	5.72
T7	31.73	25.86	10.01	26.50	7.37
T8	35.58	33.62	9.47	31.05	20.08
T9	19.36	17.82	9.96	17.07	5.08
T10	15.97	17.29	9.24	11.07	10.13
T11	14.37	16.73	12.13	9.49	7.50
T12	16.85	10.10	6.60	12.57	4.37
T13	16.12	13.20	5.25	15.88	10.63

Table 5: Maximum horizontal radial position error (in metres) at 50% confidence level

Test site	Algorithm				
	LSR	LSR NLOSMA	LBR	EKF	EKF NLOSMA
T1	14.63	11.07	4.83	12.84	6.08
T2	6.04	8.26	7.69	3.88	14.67
T3	12.24	8.68	5.38	8.89	13.59
T4	17.67	8.15	6.20	19.42	5.56
T5	7.75	6.83	20.63	11.03	10.86
T6	8.34	5.91	2.98	6.63	4.57
T7	29.14	22.46	5.21	24.86	4.62
T8	27.25	24.32	6.34	27.52	15.88
T9	14.38	5.35	8.14	13.70	4.35
T10	7.73	7.78	4.30	9.02	8.84
T11	7.90	11.69	8.48	8.25	4.76
T12	11.48	5.43	2.70	7.73	2.16
T13	12.28	8.18	4.14	14.08	7.83

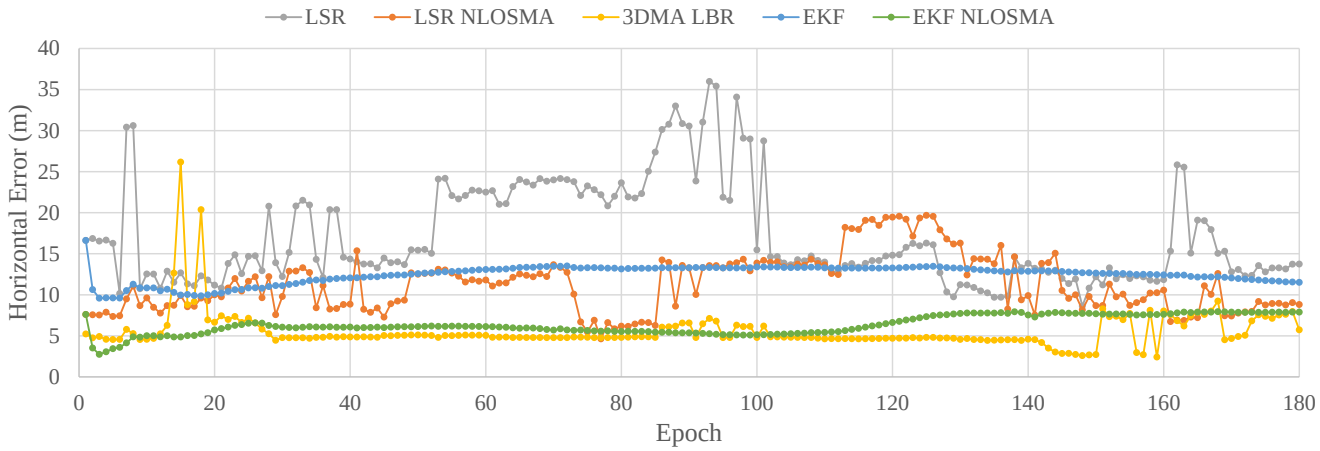

Figure 10: Horizontal position errors for the solutions of different algorithms on test site T1

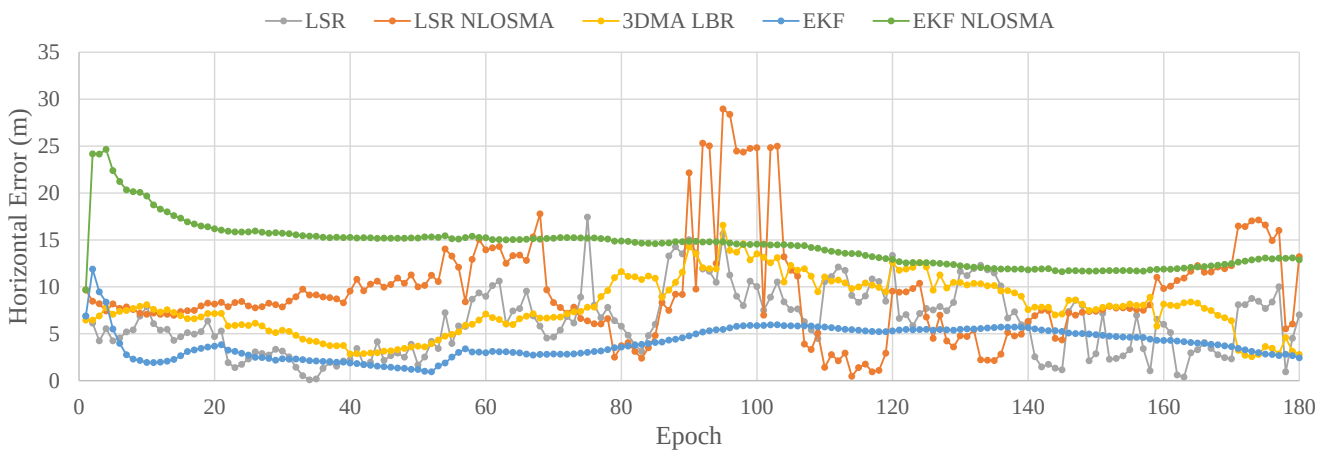

Figure 11: Horizontal position errors for the solutions of different algorithms on test site T2

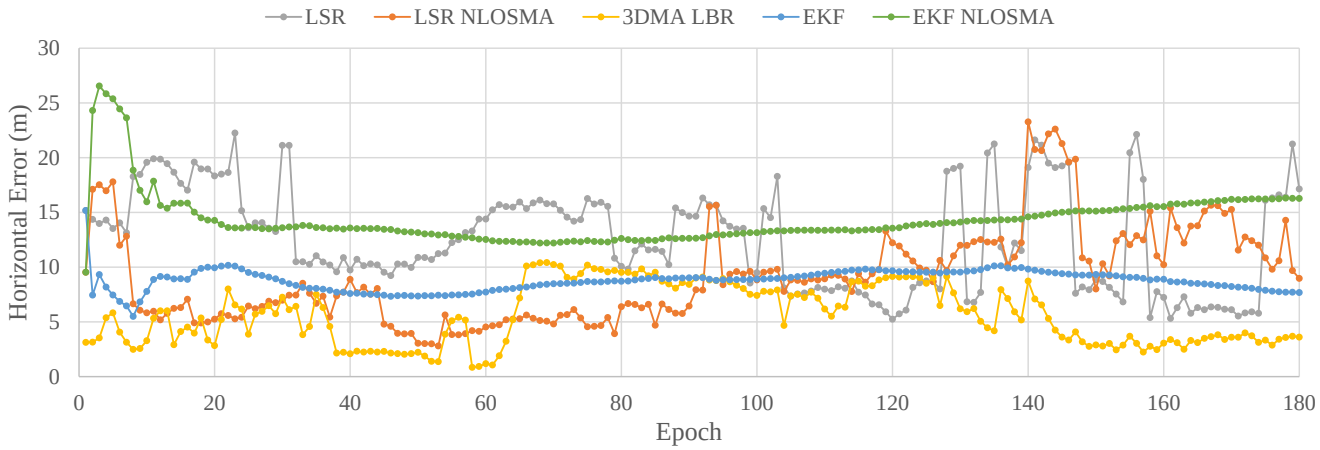

Figure 12: Horizontal position errors for the solutions of different algorithms on test site T3

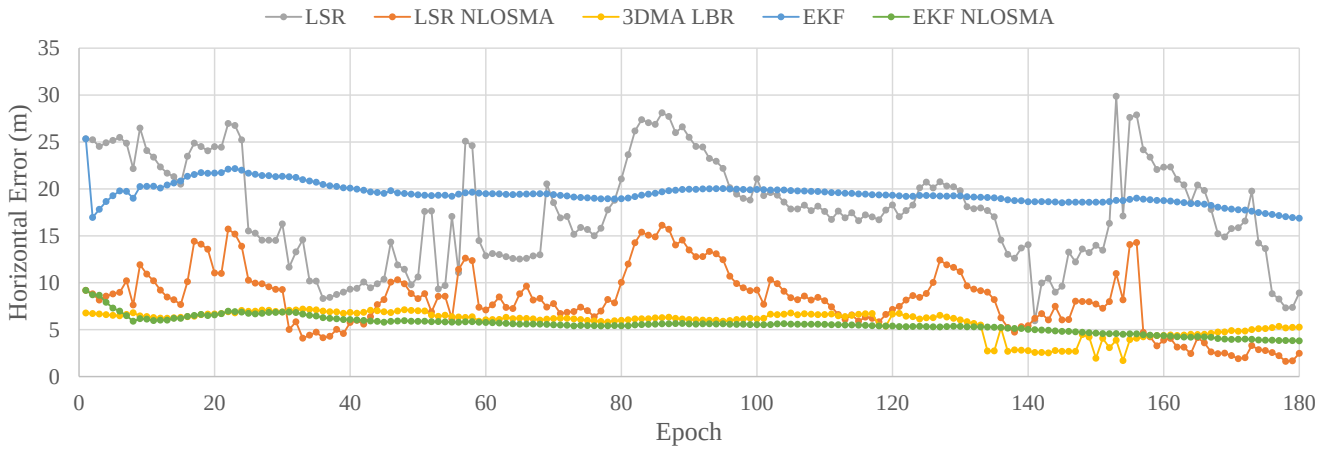

Figure 13: Horizontal position errors for the solutions of different algorithms on test site T4

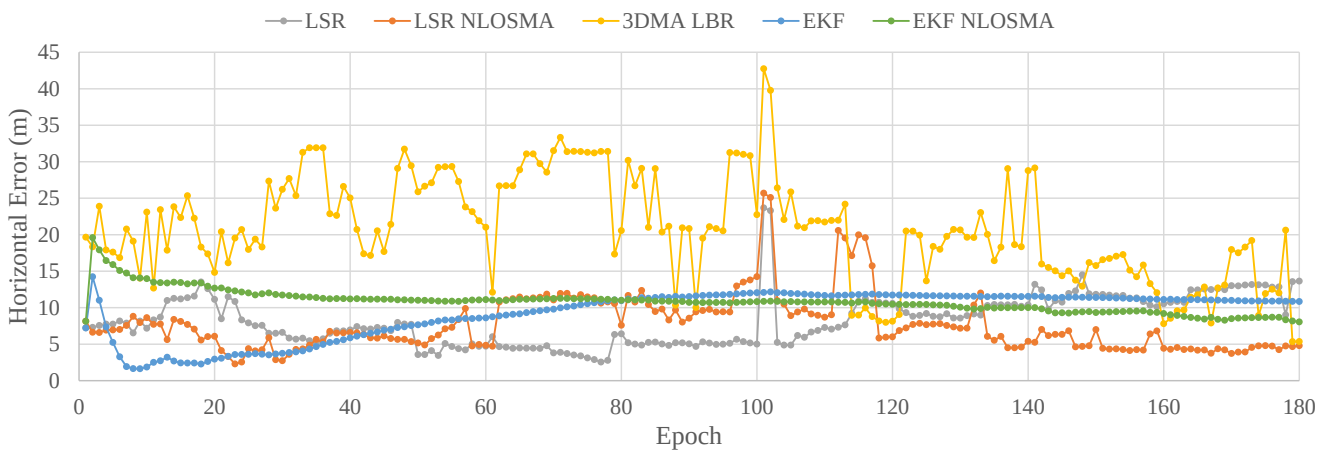

Figure 14: Horizontal position errors for the solutions of different algorithms on test site T5

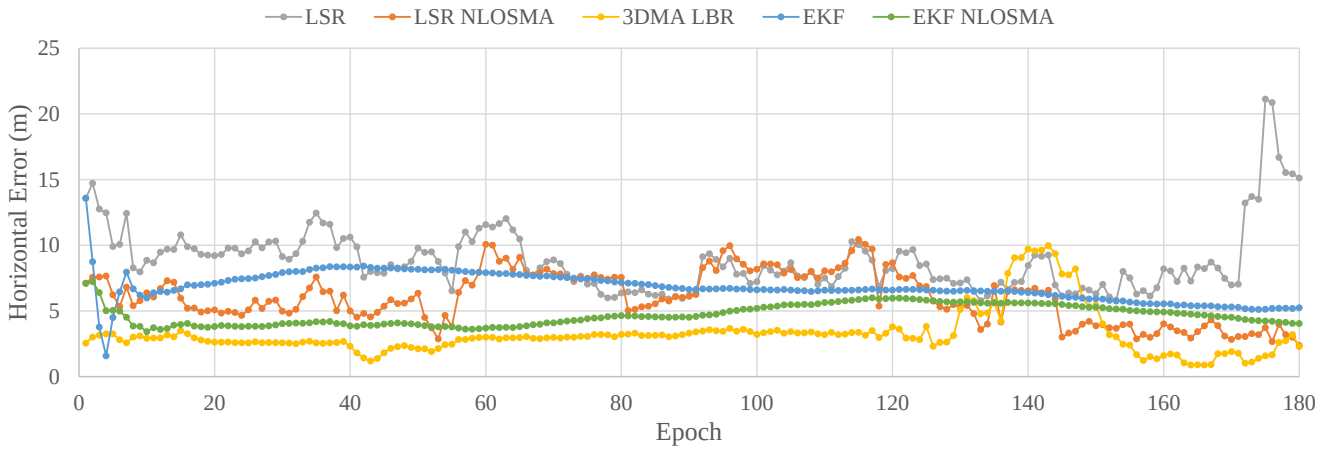

Figure 15: Horizontal position errors for the solutions of different algorithms on test site T6

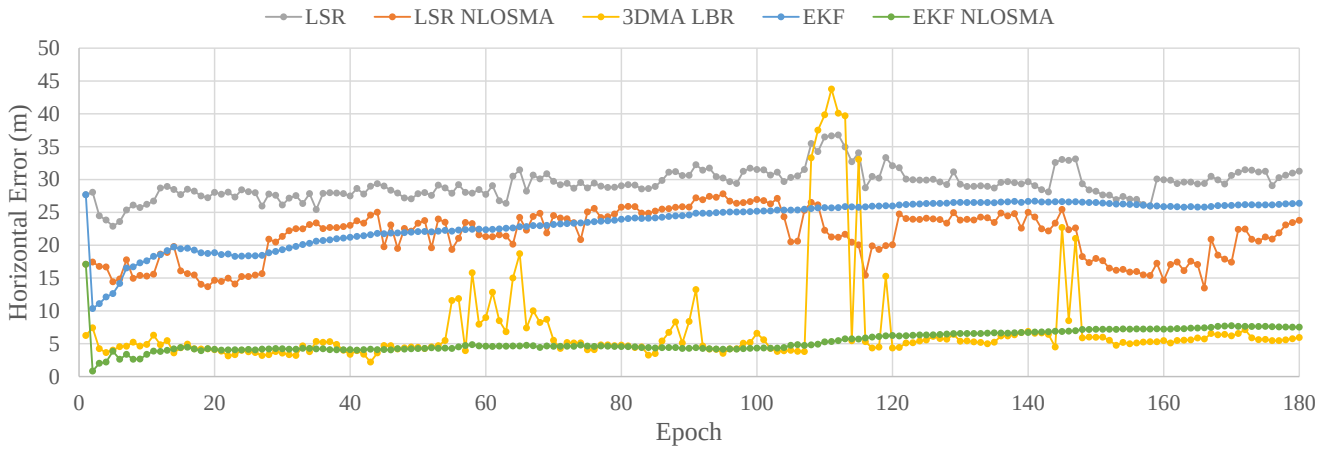

Figure 16: Horizontal position errors for the solutions of different algorithms on test site T7

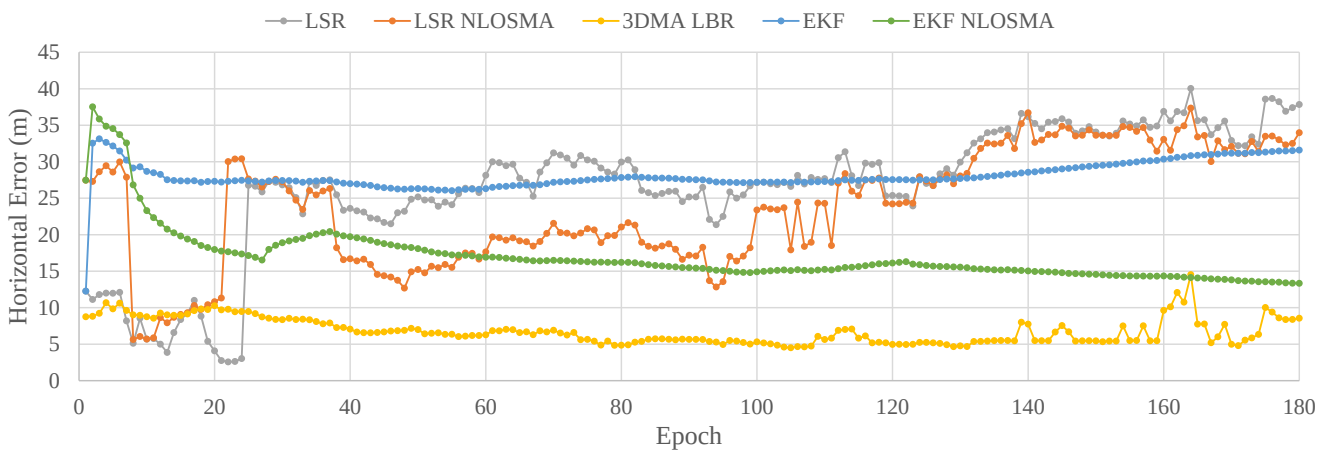

Figure 17: Horizontal position errors for the solutions of different algorithms on test site T8

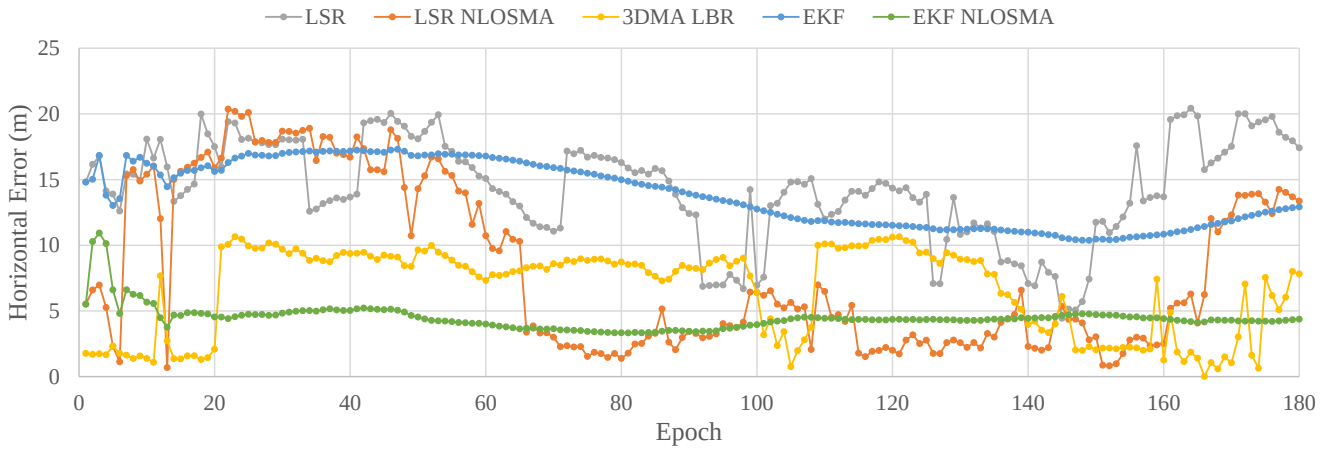

Figure 18: Horizontal position errors for the solutions of different algorithms on test site T9

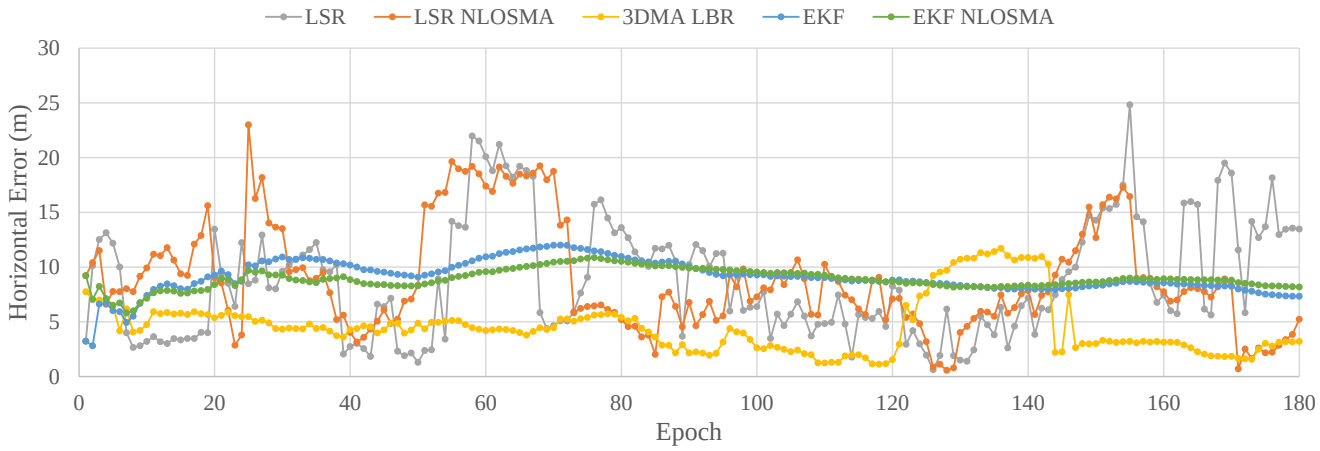

Figure 19: Horizontal position errors for the solutions of different algorithms on test site T10

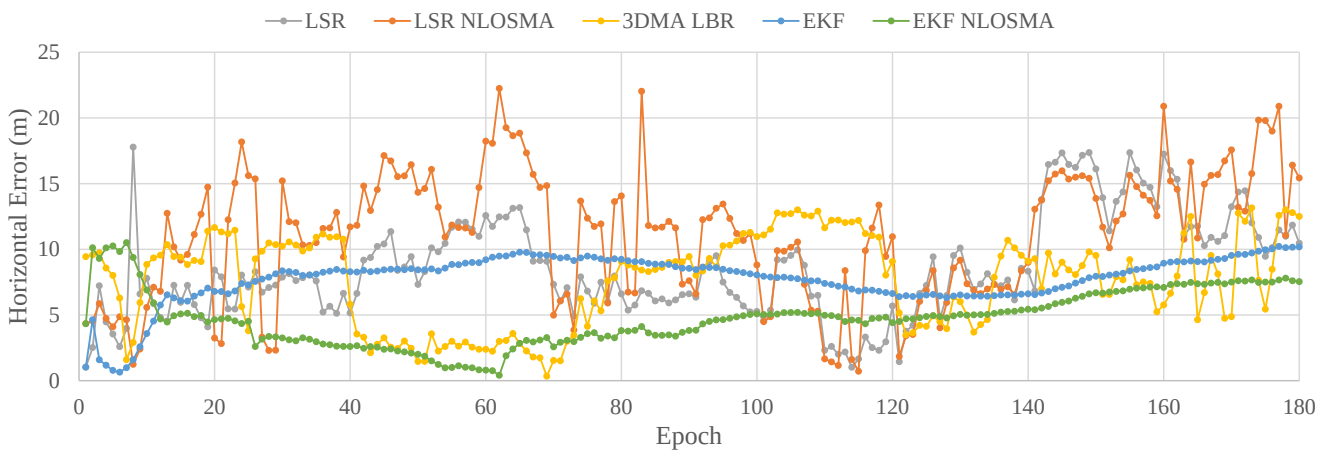

Figure 20: Horizontal position errors for the solutions of different algorithms on test site T11

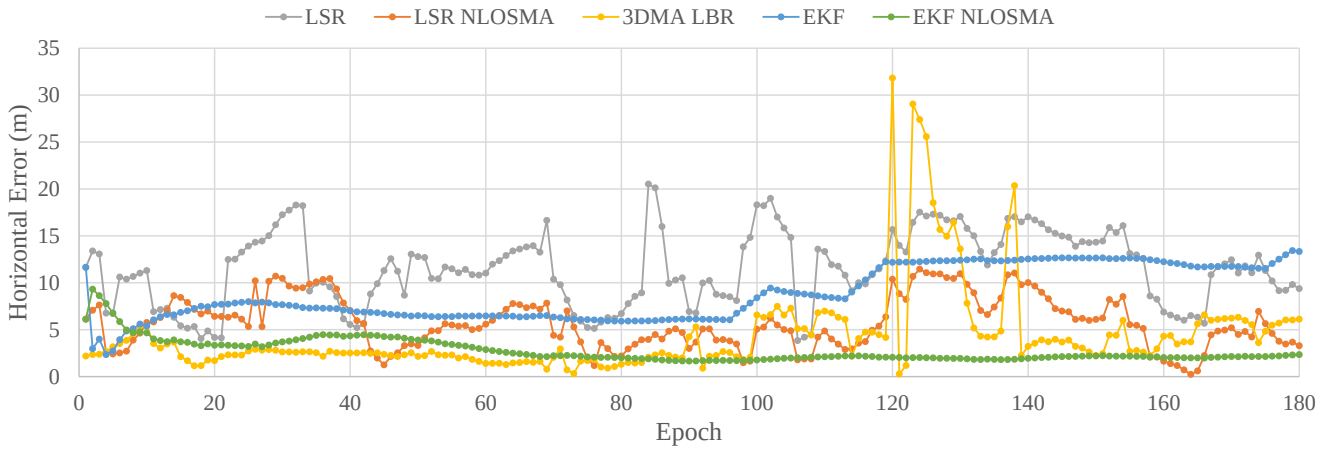

Figure 21: Horizontal position errors for the solutions of different algorithms on test site T12

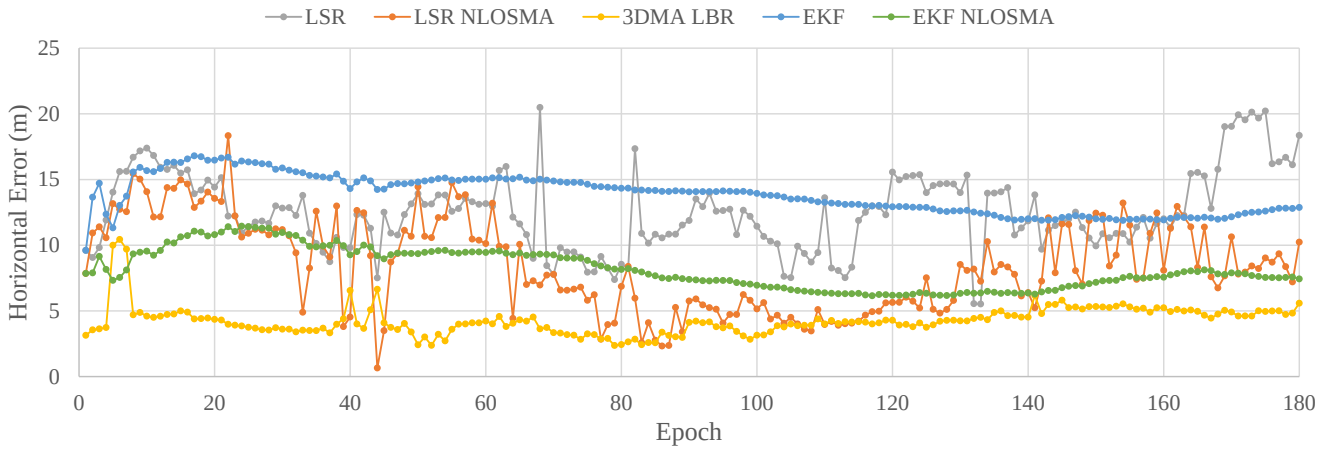

Figure 22: Horizontal position errors for the solutions of different algorithms on test site T13